The effect of abdominal wall morphology on ultrasonic pulse distortion. Part I. Measurements

Laura M. Hinkelman[a)]
Department of Electrical Engineering, University of Rochester, Rochester, New York 14627

T. Douglas Mast
Applied Research Laboratory, The Pennsylvania State University, University Park, Pennsylvania 16802

Leon A. Metlay
Department of Pathology and Laboratory Medicine, University of Rochester Medical School, Rochester, New York 14642

Robert C. Waag
Departments of Electrical Engineering and Radiology, University of Rochester, Rochester, New York 14627

(Received 14 December 1997; revised 13 July 1998; accepted 17 August 1998)

The relative importance of the fat and muscle layers of the human abdominal wall in producing ultrasonic wavefront distortion was assessed by means of direct measurements. Specimens employed included six whole abdominal wall specimens and twelve partial specimens obtained by dividing each whole specimen into a fat and a muscle layer. In the measurement technique employed, a hemispheric transducer transmitted a 3.75-MHz ultrasonic pulse through a tissue section. The received wavefront was measured by a linear array translated in the elevation direction to synthesize a two-dimensional aperture. Insertion loss was also measured at various locations on each specimen. Differences in arrival time and energy level between the measured waveforms and computed references that account for geometric delay and spreading were calculated. After correction for the effects of geometry, the received waveforms were synthetically focused. The characteristics of the distortion produced by each specimen and the quality of the resulting focus were analyzed and compared. The measurements show that muscle produces greater arrival time distortion than fat while fat produces greater energy level distortion than muscle, but that the distortion produced by the entire abdominal wall is not equivalent to a simple combination of distortion effects produced by the layers. The results also indicate that both fat and muscle layers contribute significantly to the distortion of ultrasonic beams by the abdominal wall. However, the spatial characteristics of the distortion produced by fat and muscle layers differ substantially. Distortion produced by muscle layers, as well as focal images aberrated by muscle layers, show considerable anisotropy associated with muscle fiber orientation. Distortion produced by fat layers shows smaller-scale, granular structure associated with scattering from the septa surrounding individual fat lobules. Thick layers of fat may be expected to cause poor image quality due to both scattering and bulk absorption effects, while thick muscle layers may be expected to cause focus aberration due to large arrival time fluctuations. Correction of aberrated focuses using time-shift compensation shows more complete correction for muscle sections than for fat sections, so that correction methods based on phase screen models may be more appropriate for muscle layers than for fat layers. [S0001-4966(98)05911-6]

PACS numbers: 43.80.Cs, 43.80.Vj, 43.58.Ry, 43.20.Fn [FD]

INTRODUCTION

The relationship between abdominal wall tissue structure and image quality in transabdominal ultrasonography is a subject of considerable lore and speculation. For instance, a widely held belief among clinical ultrasonographers and ultrasound researchers is that poor ultrasonic image quality is primarily associated with obesity.[1–3] Although this belief has some scientific basis, at least because increased body wall thickness should cause greater attenuation of the ultrasound beam in transabdominal imaging, most of the evidence supporting this theory is anecdotal. Some clinicians and researchers maintain that poor ultrasonic image quality does not directly correspond to obesity in general, that is, that image quality depends on the individual's body wall structure. For example, while many obese individuals are difficult to image, some thin but muscular individuals also produce poor ultrasonic image quality.[4,5] Very little scientific study has been conducted to relate the characteristics of abdominal wall morphology to ultrasonic aberration.

In one clinical study,[5] the quality of abdominal B-scans from 140 people was correlated with various body characteristics. Although obesity was associated with poor image quality in this study, it was not considered to be a direct cause of reduction in image quality. In most cases, the upper

[a)]Current address: Department of Meteorology, The Pennsylvania State University, University Park, Pennsylvania 16802.

layers of the abdominal wall imaged well, even when the deeper organs were obscured in the images. For this reason, the authors suggested that muscle may contribute significantly to the formation of distortion. Other factors associated with poor images included atherosclerosis, lower limb paralysis, and the presence of ribs, intestinal gas, or an aponeurosis (tissue joining two muscle groups) in the acoustic path.

Several groups have studied the importance of fat and muscle layers by using pork tissue to simulate the human abdominal wall.[3,6,7] In the study reported in Ref. 6, pork fat and a combination of pork fat and muscle were found to decrease mean grey level in ultrasonic images of a tissue-mimicking phantom. In addition, a thick layer of fat was observed to produce an ''unsharp image,'' while muscle alone seemed to have little effect on image quality. In a related study,[7] signals were received from a disc transducer placed in the thoracic cavity of an anesthetized pig by a phased array outside the pig's abdomen. The pig's abdominal wall was removed in sequential layers, and images were made at each depth. Removal of the complete abdominal wall resulted in significant improvement of image quality, but no individual layer was found to cause the bulk of the image degradation. Instead, removal of each consecutive layer resulted in an incremental reduction of distortion.[5] In a similar *in vitro* study,[3] separate pork fat and muscle samples were found to slightly raise the sidelobe levels of an ultrasonic beam at human body temperature. Similar levels of distortion were measured for a larger sample, containing a layer of fairly homogeneous muscle and two layers of fat. Much higher levels of distortion were detected for another specimen in which the muscle was marbled with fat.

Some insight into the relationship between distortion caused by animal tissues and the human abdominal wall is provided by the study reported in Ref. 8. In this study, samples of pork muscle, pork fat, and a combination of these did not produce distortion similar to that measured for the human abdominal wall. However, heavily marbled beef did cause significant distortion, including both phase and wave shape aberrations. Simple time-shift compensation was unable to improve images subjected to distortion produced by heavily marbled beef or by the human abdominal wall. These results, considered together with those from Refs. 3, 6, and 7 above, show that studies of ultrasonic distortion caused by animal tissue should be interpreted with caution when characterization of ultrasonic distortion effects in humans is desired. The studies indicate that animal tissues may not, in general, accurately mimic ultrasonic distortion processes occurring in human tissues, but that certain animal tissues (e.g., muscle tissue that is marbled with fat[3,8]) may provide reasonable approximations.

Taken together, published studies provide mixed experimental evidence that tissue structures other than fat significantly contribute to ultrasonic distortion in the human body wall. Since the prospects for adaptive correction of ultrasonic aberration depend on both the physical causes of the distortion and the locations at which the distortion is incurred, it is important that the source of wavefront distortion be accurately known. For example, if both fat and muscle layers cause significant distortion, single phase screen models[9–15] may be inappropriate for modeling distortion through the abdominal wall. Likewise, if internal structure within the layers of the human abdominal wall proves to be important to ultrasonic image degradation *in vivo*, correction algorithms based on homogeneous-layer models[4,16,17] will provide suboptimal improvement in image quality.

One barrier to understanding wavefront distortion mechanisms has been an apparent lack of information regarding the structure of the human abdominal wall and the type of distortion this morphology could be expected to produce. For example, tissues such as fat and muscle are commonly assumed to be homogeneous rather than possessing internal structure.[4,9,16,18–20] Both muscle and fat are, in fact, comprised of smaller tissue units organized together.[20–22] For this reason, fat and muscle layers can both produce distortion. Since the structures are different, distortion produced by these two tissues may be expected to have different spatial characteristics. Such differences have been observed in some experimental studies involving sections of the human abdominal wall.[23] A related study of simulated ultrasonic propagation through human abdominal wall cross sections[24,25] suggests that muscle and fat affect propagating ultrasonic wavefronts differently. This study also indicates that ultrasonic wavefront distortion is caused by a combination of strong scattering and large-scale sound-speed variations.

The present paper reports an experimental study of the relative effects of the muscle and fat layers of the abdominal wall on ultrasonic pulses. The purpose of this study was to investigate how specific morphologic features of the abdominal wall affect ultrasonic image quality. Answers to this question, provided in part by this paper and the companion simulation paper,[26] will help to determine the types of correction procedures that are most effective and the limitations of these procedures.

I. ABDOMINAL WALL ANATOMY

Most previous models of tissue structure employed in medical ultrasound have been based on oversimplifications of human anatomy. Accurate understanding of abdominal wall morphology is critical to the development of meaningful models for ultrasound–tissue interactions in the abdominal wall, as well as to the development of improved algorithms for aberration correction in ultrasonic imaging. For these reasons, the morphologic features of the abdominal wall relevant to medical ultrasonic imaging are summarized below. This description of the abdominal wall is employed in this study to interpret measured distortion from whole abdominal wall specimens as well as individual fat and muscle layers. The already noted companion paper[26] employs this description as the basis for the propagation model used in the simulations reported there. Further details can be found in standard references on human anatomy such as Refs. 21, 22, and 27.

A typical abdominal wall specimen used in this study (specimen 101a) is shown in Fig. 1. The skin, fat, and muscle sections are readily apparent in the view showing the skin surface [Fig. 1(a)]. In this case, the fat layer is more than

FIG. 1. Abdominal wall specimen 101a before dissection. (a) View with skin facing upward. (b) View with peritoneum and retroperitoneal fat facing upward. Markings are at intervals of 1 cm.

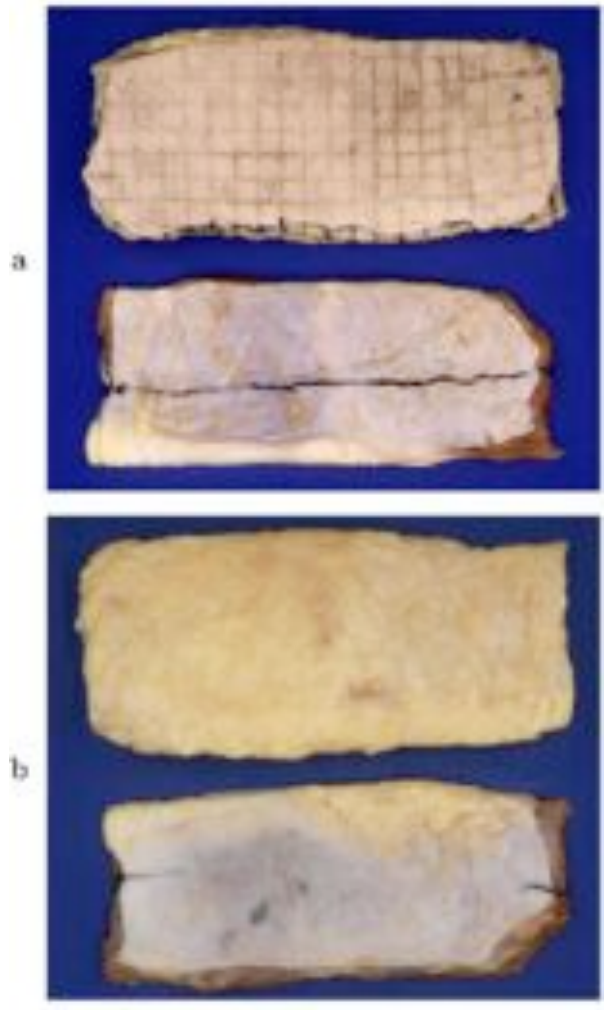

FIG. 2. Individual layers of abdominal wall specimen 113. (a) Views showing skin in the fat section (above) and fascia in the muscle section (below). (b) Views of the opposite sides of each layer, showing subcutaneous fat in the fat section (above) and the peritoneum with retroperitoneal fat in the muscle section (below).

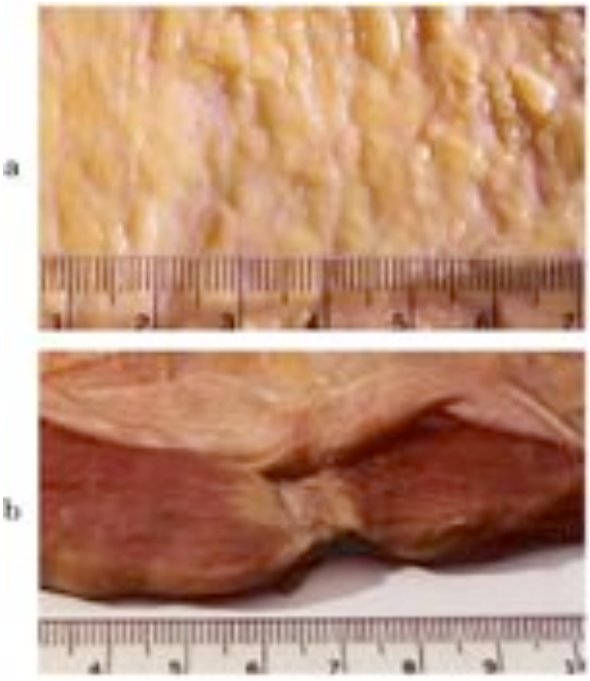

FIG. 3. Magnified view of abdominal wall features in specimen 65. (a) Subcutaneous fat lobules. (b) Muscle layer, with peritoneum drawn back to expose an aponeurosis.

twice the thickness of the muscle layer. The black lines are remnants of markings used to position the tissue in measurements. The opposite side of the same specimen [Fig. 1(b)] shows a clear view of the peritoneum, the thick membrane that lines the inner surface of the abdominal wall. It is also apparent that the muscle layer is not uniform. In this case, a portion of the muscle section consists largely of fat. Some retroperitoneal fat is also evident in the back left corner of the specimen. Even with this fat section attached under the peritoneal membrane, however, the peritoneal surface appears smooth, as does the skin surface.

The muscle and fat sections of specimen 113 are shown after separation in Fig. 2. Panel (a) shows the fat section with the skin facing upward and the muscle section in the same orientation, exposing the sheet of connective tissue that separated the layers. Since the surface of this membrane was originally attached to both the fat and muscle layers, the fat–muscle interface was smooth before dissection. Although the layers do not separate absolutely cleanly, the surface irregularities caused by the separation are small. An aponeurosis (sheet of tissue joining two muscle groups) appears as a light-colored vertical band visible through the membrane in the muscle section. Panel (b) depicts the underside of the fat layer, revealing lobules of subcutaneous fat, as well as the underside of the muscle section, showing the peritoneum and some retroperitoneal fat.

A closer view of fat structure in specimen 65 is given in panel (a) of Fig. 3. Although fat cells contain solidified drops of oil, fat tissue is shown in panel (a) to have additional structure. Subcutaneous fat is composed of loose fat cells held together in lobules by thin septa of fibrous tissue. The lobules are usually 2.5–7.5 mm across and are approximately ovoid or spherical. In the illustration, ovoid lobules

appear to be oriented with long axes parallel to each other. The subcutaneous fat layer of the human abdominal wall is commonly 0.5–6.0 cm thick. The thickness may vary slowly with position across the abdomen. As mentioned above, fat can also occur below the peritoneum or as deposits within muscle. The speed of sound in fat is about 1.48 mm/μs at body temperature.[24]

Collagen-containing materials that connect and support organs and tissues of the body are termed connective tissue. The various connective tissue structures serve as surfaces to which the other tissues bind and thus give form to the body. The skin and aponeuroses are examples of dense connective tissue while the membranes that surround fat lobules are a form of loose connective tissue. The skin is composed of a lower layer, the dermis, which is composed of dense collagenous connective tissue, and a thin upper layer, the epidermis. The skin has approximately uniform thickness for each specimen but varies from 1–3 mm thick among individuals. Aponeuroses, which join muscle sections, are made up of highly organized dense collagenous connective tissue. The connective tissue fibers in aponeuroses run parallel to the lines of stress in the body. Tendinous intersections in the rectus abdominus, like that shown in Fig. 3(b), may be considered aponeuroses, although they tend to be less substantive. In the specimens we have examined, the connective bands in the rectus abdominus have been dominated by fat, probably because of the age of the specimen donors. Other connective tissue in the abdominal wall includes extensive sheets known as fasciae that envelop bundles of muscle fibers and are somewhat looser than aponeuroses. The peritoneal lining also rests on a thin layer of dense connective tissue. A nominal sound speed value previously employed for skin, fascia, and membranes within the abdominal wall is 1.613 mm/μs.[24]

Muscle cells, which are tubular and fluid filled, with complex fibrils, are bound into bundles by collagenous tissue. The fibrous structure of muscle tissue can be observed in Fig. 3(b). Small bundles of muscle fibers are bound together to form larger groups, including the rectus abdominus and the external, internal, and transverse obliques. Because of the arrangement of muscle groups and their segmentation, the overall muscular structure varies throughout the abdominal wall. In addition, muscles are not homogeneous as they can have fatty infiltrations (analogous to ''marbling'' in beef) and variable connective tissue content in addition to fasciae and aponeuroses. A typical sound speed for muscle, measured perpendicular to the fibers, is 1.547 mm/μs.[24]

The relative positions and orientations of muscle groups appearing in the human abdominal wall are sketched in Fig. 4 and briefly described below. The rectus abdominus,

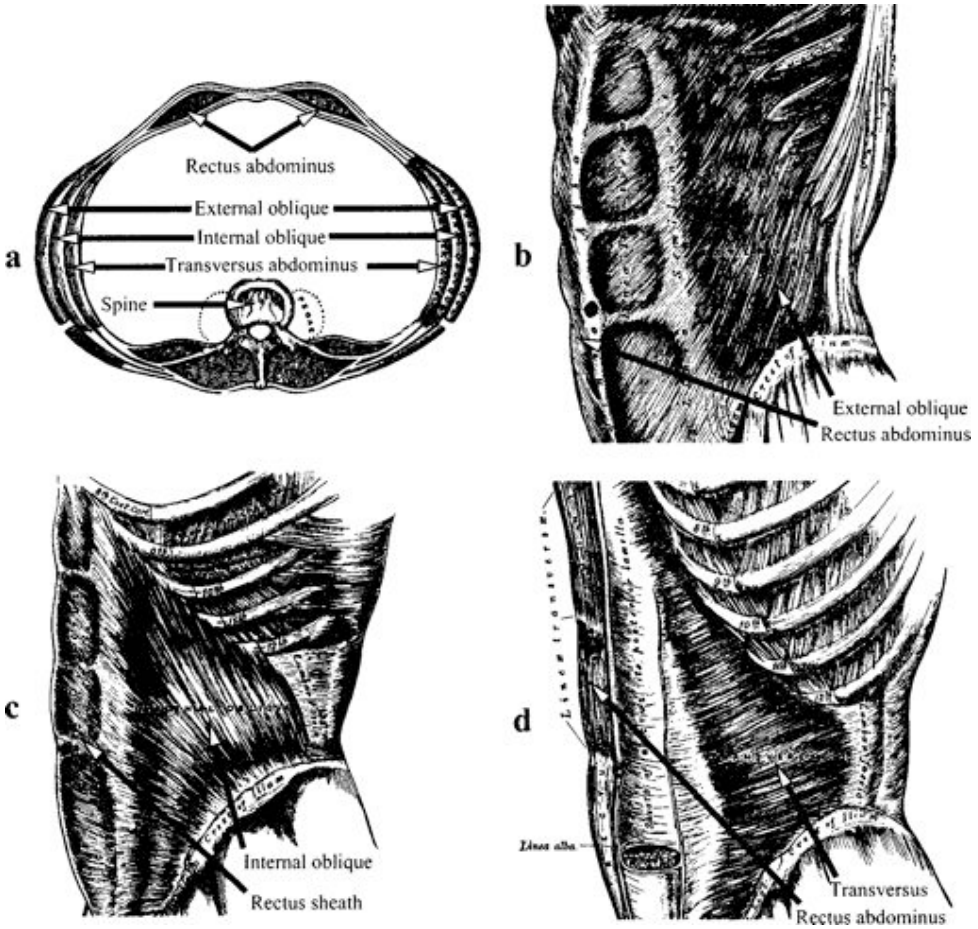

FIG. 4. Sketch of muscle groups in the human abdominal wall. (a) Cross section showing relative positions of all muscle groups. (b) External oblique and rectus abdominus. (c) Internal oblique and rectus sheath. (d) Transversus abdominus (transversalis), rectus sheath, and rectus abdominus (to left of linea alba). Adapted from Ref. 27.

whichconsists of two bands of muscle running vertically along the midline of the abdominal wall, is separated into sections by at least three horizontal or zigzagged aponeuroses. The rectus abdominus is enclosed by layers of connective tissue, called the rectus sheath. At both medial (outer) margins of the rectus muscles, the rectus sheath joins the aponeuroses of the internal and external oblique groups. Muscle fibers of the external oblique group run diagonally downward and inward from the side of the torso below the arm to their aponeurosis. The internal obliques, which lie beneath the external obliques, run diagonally upward and inward from the iliac crest to their own aponeurosis or to the ribs. The fibers of the external obliques are roughly perpendicular to those of the internal obliques. The transversus abdominus muscles lie below the internal obliques and are oriented approximately horizontally. At the midline of the body, between the rectus abdominus muscles, is the linea alba, where the peritoneum joins with the aponeuroses of the internal and external obliques and the transversus abdominus as well as with other connective fasciae. In this region and just beyond the medial margins of the rectus abdominus, there is usually no muscle present in the abdominal wall.

The abdominal wall also contains a variety of blood vessels which generally lie in the plane of the abdominal wall. Blood vessels are present in a range of sizes and are composed primarily of connective tissue and muscle. Other smaller components of the abdominal wall, such as nerves and hair follicles, are neglected in this study.

II. METHOD

A. Measurements

Six fresh unfixed specimens of the upper abdominal wall were obtained from autopsy and stored at −20°C. The six specimen donors ranged in age from 57 to 85 with an average age of 71 years. Four died of cardiac failure, one of stroke, and the last of Alzheimer's disease. Five of the donors were male and one was female. None of the donors was significantly overweight.

Each specimen was thawed by immersion in room-temperature saline solution and reference lines for positioning were ruled on the specimen surface with India ink. The specimen was then pressurized to 345 MPa (500 p.s.i.) for one half-hour to ensure that no air bubbles were present within the tissue. (This pressurization technique has previously been shown to remove bubbles that cause significant ultrasonic scattering.[28,29]) The wavefront distortion produced by the whole specimen was then measured using the procedure and equipment detailed in Ref. 30 and highlighted here for convenience. The specimen was suspended with the skin upward between 7.5-μm-thick polyimide membranes in a water tank electronically maintained at 37.0°C. Ultrasonic pulses with a nominal center frequency of 3.75 MHz were emitted from a custom-made, 13-mm-diam hemispheric source placed approximately 165 mm below the specimen. Data were recorded on each of the 128 elements of a 3.75-MHz linear array positioned 5–10 mm above the specimen's skin surface. A foam mask was used to reduce the elevation dimension of the receiving array, so that the active area of each element measured 0.72×1.44 mm^2. The array was physically translated 32 times in the elevation direction to obtain data for a 92.16×46.08 mm^2 aperture. The position of each measurement relative to the markings on the specimen's skin was noted. The peak-to-peak insertion loss of the specimen was also measured in several locations by comparing waveform maxima for signals recorded through the tissue and through a water path.

After distortion data had been collected for the entire specimen, the specimen was removed from the measurement chamber and separated into two sections. This was accomplished by carefully dividing the specimen at the septum between the subcutaneous fat and the muscle layer with a scalpel. In general, the distinction between those layers was quite clear. However, because the septum itself is thin, it was not divided but remained entirely with one of the layers, whichever proved easier at the time. During this dissection, care was taken not to disturb the markings on the skin. Additional markings were added on the top surface of the muscle layer corresponding to those on the skin. The first of the resulting sections contained the skin and subcutaneous fat, and will be referred to as the ''fat'' section. The other consisted of the remainder of the specimen from beneath the subcutaneous fat down to and including the parietal pleura. This section consisted mainly of muscle but also included fatty intrusions, blood vessels, and connective tissue. This section will be referred to as the ''muscle'' section.

Distortion measurements were made for the individual layers. The protocol used was the same as that described for the intact specimens. The muscle layer was measured first. It was inserted with the mount at the same height as was used for the whole specimen, so that the distance between the layer and each transducer was the same for this layer as when the muscle layer was part of the whole specimen. When the fat layer was measured, the mount was placed as before but the receiving transducer was lowered to ensure that the separation of the receiver and the skin surface was the same as in the original measurement. This allowed the configuration to be maintained as much as possible without requiring extensive changes between measurements. The resulting small reduction in distance between the source and specimen did not significantly affect the measurements because the hemispheric source transducer induced an incident field comparable to that of a point source far from the specimen. The India ink marks on the surface of each muscle and fat layer were used to align the layer laterally in the mount as it had been for the original whole specimen measurement.

Water path measurements were made before and after each specimen measurement series to serve as a reference and to characterize system effects.

B. Data processing

The received wavefronts were characterized as in previously reported measurements.[31] The processing methods are briefly summarized here. A reference waveform was created for each set of data by averaging those waveforms that met a cross-correlation criterion for similarity. This reference pulse was cross-correlated with all the measured waveforms to produce an arrival time surface from which questionable out-

lying points were removed by smoothing. A two-dimensional fourth-order polynomial fit to the arrival time surface was used to window the original waveforms. A new arrival time surface was then obtained by repeating the arrival time estimation procedure using the windowed data. The effects of measurement geometry were removed by subtracting a best (least mean square error) fit two-dimensional fourth-order polynomial from the calculated arrival times to yield the arrival time fluctuations across the aperture. Energy level variations were calculated by integrating the squared amplitudes of the samples in each windowed waveform, converting the results to decibel units, and subtracting a fitted two-dimensional, fourth-order polynomial from the result. The waveform similarity factor[12] was computed using all the windowed waveforms throughout the aperture to provide a measure of the variability of waveform shape characteristics.

The arrival time and energy level variations determined for each data set, including the whole and sectioned specimens, were displayed as two-dimensional grayscale plots and their magnitude was described by computation of rms values. The spatial variability of the maps was described by the full-width half-maximum correlation lengths of the arrival time fluctuations and the energy level fluctuations in the array and elevation directions. To characterize anisotropy of wavefront distortion, aspect ratios were computed in each case as the ratio of the larger correlation length to the smaller correlation length. Average insertion loss values for the specimens were also computed.

Wavefronts were synthetically focused using a direct implementation of the time-domain Rayleigh integral. In this method, the time history of an ultrasonic pressure field is calculated in an image plane located 180 mm from the receiving aperture. Received wavefronts were spatially apodized using Hamming windows in elevation and azimuth. Waveforms from individual array elements, modeled as monopole sources on an infinite rigid baffle, were then combined according to the formula[32]

$$p(x,y,t)=\frac{\rho}{2\pi}\int\int\frac{\dot{v}_n(x_s,y_s,t-R/c+R_0/c)}{R}\,dx_s\,dy_s, \tag{1}$$

where $p(x,y,t)$ is the acoustic pressure in the image plane, ρ is the ambient density, $v_n(x_s,y_s,t)$ is the normal velocity in the source plane (defined here to be directly proportional to the waveform signal), and $R=\sqrt{(x-x_s)^2+(y-y_s)^2+z^2}$ is the distance from a point (x,y,z) in the image plane to a point $(x_s,y_s,0)$ in the source plane. An additional delay, represented in Eq. (1) by the distance $R_0=\sqrt{x_s^2+y_s^2+z^2}$, causes the wavefront to be focused at the center of the image plane at the time $t=0$. The geometry for the synthetic focusing implementation is essentially that sketched in Fig. 1 of Ref. 11.

In the numerical implementation of Eq. (1), the time derivative $\dot{v}$ was evaluated using the second-order-accurate finite difference expression

$$\dot{v}(x_s,y_s,t)\approx\frac{v(x_s,y_s,t+\Delta t)-v(x_s,y_s,t-\Delta t)}{2\Delta t}, \tag{2}$$

where Δt is the sampling time of 0.05 μs. Focal-plane waveforms were then computed by evaluating the integral in Eq. (1) as a discrete summation over all the aperture elements. Linear interpolation of source waveforms was employed to combine signals at common instants in the image plane. Pressure time histories were computed for 128 temporal samples, 120 image points in the aperture direction, and 80 image points in the array direction, using a time step of 0.05 μs and a spatial step of 0.4688 mm.

Focal quality was evaluated using effective widths in the array, azimuth, and time directions for levels -10 and -20 dB down from the peak amplitude. These effective widths were calculated using maximum-amplitude projections of analytic envelopes for the pressure signals, as in Ref. 11. Peripheral energy ratios, defined as the ratio between the integrated pulse energy outside a reference ellipsoid to the integrated pulse energy inside the ellipsoid,[11] were calculated for the -10-dB effective widths. As in Ref. 11, the reference ellipsoid was defined to be centered at the position of peak amplitude and the ellipsoid width along each axis was equal to the -10-dB effective width in the corresponding direction.

III. RESULTS

Arrival time and energy level fluctuation maps for the measured muscle, fat, and whole abdominal wall sections are shown in Fig. 5. The distortion produced by the fat and muscle layers have distinctly different spatial characteristics. The muscle layers produce distortion patterns having clearly oriented features. In most cases, a pattern of parallel striations is present. This is frequently overlaid with a few high-contrast curvilinear features, generally perpendicular to the underlying striations. The arrival time and energy level fluctuation maps for the fat layers, on the other hand, appear to consist almost entirely of small granular structures. On the scales used here, the energy level fluctuation maps display higher contrast when compared to the arrival time fluctuation maps. The maps for the whole specimens combine the characteristics of both layers in varying proportions. The striations and strong patterns of the muscle fluctuation maps are blended with the granular patterns caused by the fat layer. Shifts in locations of features in the whole and section distortion maps are mainly attributed to slight differences in specimen position in the sequential layer measurements.

The differences in the distortion maps produced by the different tissue sections are closely related to the differences in the structure of these layers. Inspection of the specimens indicated that most striations seen in the muscle layer distortion maps run parallel to muscle fibers. The white bands correspond to the positions of aponeuroses at the muscle connection points. Similarly, the granular patterns of the fat distortion maps are reminiscent of the arrangement of fat lobules. The results for the whole specimens contain features present in the results for each of the corresponding individual sections. These observations lead to the simple conclusion that the spatial characteristics of distortion produced by tissue structures resemble projections of the structures themselves.

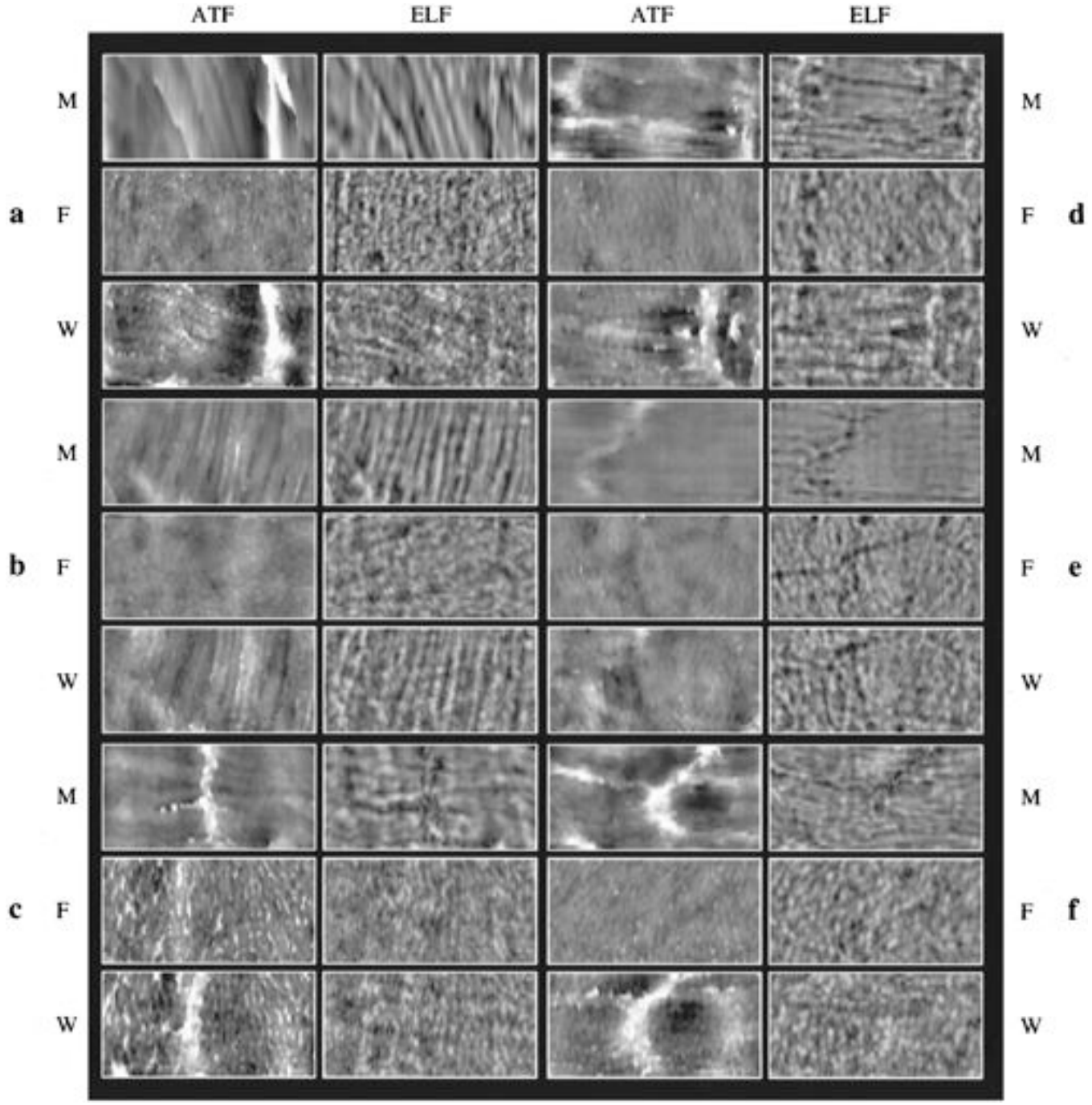

FIG. 5. Distortion maps for six abdominal wall specimens and their individual muscle and fat layers. Energy level fluctuations (ELF) and arrival time fluctuations (ATF) are shown for the muscle layers (M), fat layers (F), and whole specimens (W). The ATFs are shown on a linear gray scale with white indicating a delay of 150 ns and black indicating an advance of 150 ns. Log-compressed ELFs are shown on a gray scale with white indicating an increase of 10 dB and black indicating a decrease of 10 dB. Each panel spans 128 elements (92.16 mm) in the horizontal (array) direction and 32 elements (46.08 mm) in the vertical (elevation) direction. (a) Specimen 65. (b) Specimen 101. (c) Specimen 113. (d) Specimen 114. (e) Specimen 116. (f) Specimen 118.

The statistics given in Table I quantitatively describe the distortion illustrated in Fig. 5. Mean distortion values for five water path measurements, which characterize the influence of the measurement system, are also given for comparison. The aspect ratios of the distortion produced by the muscle layers (mean values 1.84 for arrival time fluctuations and 2.50 for energy level fluctuations) reflect the anisotropy evident in the distortion maps. The correlation lengths for arrival time fluctuations produced by the muscle sections are greater than those for the energy level variations. The distortion maps produced by the fat layers are also somewhat anisotropic: average aspect ratios for the arrival time and energy level fluctuations are 1.54 and 1.45, respectively. Although some anisotropy may result from the element dimensions (the array direction pitch was half the elevation direction pitch), the computed aspect ratios are consistent with the ovoid appearance of fat lobules seen in Fig. 3. Correlation lengths for fat layers are significantly smaller than those for the muscle layers and are not preferentially aligned with respect to the muscle fibers. This decrease in correlation

TABLE I. Wavefront distortion statistics for measured propagation. Statistics shown include specimen thicknesses, rms arrival time and energy level fluctuations, correlation lengths (CL) of fluctuations in the array (x) and elevation (y) directions, aspect ratios (AR) of correlation lengths, and waveform similarity factors. The mean and standard deviation values shown for correlation lengths (marked with asterisks) are statistics for the larger and smaller correlation lengths, respectively, in each measurement.

			Arrival time fluctuations				Energy level fluctuations				
Specimen	Layer	Thickness (mm)	rms (ns)	CL_x (mm)	CL_y (mm)	AR	rms (dB)	CL_x (mm)	CL_y (mm)	AR	Waveform similarity factor
	muscle	8.5	60.3	5.40	17.18	3.18	3.07	2.45	8.41	3.43	0.951
65	fat	9.8	31.1	1.51	2.17	1.44	3.85	1.55	2.14	1.38	0.946
	whole	18.3	75.9	6.35	11.78	1.86	3.45	2.15	1.95	1.10	0.887
	muscle	7.8	28.5	3.31	7.16	2.16	2.94	2.08	5.28	2.54	0.939
101	fat	13.0	26.8	6.07	5.53	1.10	2.78	2.86	2.00	1.43	0.947
	whole	20.8	39.0	5.12	8.86	1.73	3.05	2.13	3.34	1.57	0.912
	muscle	12.0	44.5	6.51	7.87	1.21	2.91	4.20	2.84	1.48	0.931
113	fat	17.8	51.6	1.38	2.57	1.86	2.68	1.30	2.30	1.77	0.802
	whole	29.8	70.3	2.60	4.67	1.80	3.01	1.58	2.44	1.54	0.807
	muscle	10.0	55.8	7.98	6.18	1.29	3.19	4.41	1.85	2.38	0.921
114	fat	17.5	21.5	1.96	3.94	2.01	2.85	2.26	3.71	1.64	0.956
	whole	27.5	54.0	4.43	5.86	1.32	3.35	3.23	2.51	1.29	0.880
	muscle	8.3	18.9	8.58	5.22	1.64	1.86	4.77	1.63	2.93	0.981
116	fat	9.5	21.9	3.18	4.90	1.54	2.88	1.99	2.53	1.27	0.965
	whole	17.8	35.6	6.01	6.19	1.03	3.09	2.23	2.43	1.09	0.949
	muscle	18.0	61.9	10.15	6.49	1.56	2.75	3.94	1.76	2.24	0.919
118	fat	14.3	23.5	1.65	2.11	1.28	2.71	2.07	2.46	1.19	0.914
	whole	32.3	61.4	9.46	7.56	1.26	2.95	2.09	2.29	1.10	0.862
	muscle	10.8	45.0	9.82*	5.52*	1.84	2.79	5.17*	2.10*	2.50	0.940
Mean	fat	13.7	29.4	3.63*	2.54*	1.54	2.96	2.67*	1.86*	1.45	0.922
	whole	24.4	56.0	7.81*	5.35*	1.50	3.15	2.65*	2.08*	1.28	0.883
	water	⋯	6.0	⋯	⋯	⋯	0.70	⋯	⋯	⋯	0.991
	muscle	3.9	17.8	3.74*	1.21*	0.74	0.48	1.66*	0.46*	0.66	0.023
Standard	fat	3.6	11.5	1.63*	1.61*	0.35	0.44	0.57*	0.36*	0.22	0.061
deviation	whole	6.2	16.4	2.68*	1.72*	0.34	0.20	0.51*	0.31*	0.23	0.048
	water	⋯	0.8	⋯	⋯	⋯	0.07	⋯	⋯	⋯	0.001

length reflects the relative size and shape of fat lobules and muscle fibers as well as the absence of strong linear distortion features, such as those produced by aponeuroses in the muscle layer, from the fat layer distortion maps.

The data in Table I indicate that arrival time fluctuations caused by muscle layers are significantly more severe than those caused by fat layers. The average rms arrival time fluctuation for muscle layers is 45.0 ns versus 29.4 ns for fat. Fat layers produce slightly more energy level distortion than the muscle layers. The arrival time and energy level distortion produced by whole specimens is generally greater than that produced by the individual layers. The arrival time fluctuations are typically comparable to the geometric sum of the rms arrival time distortion values of the individual layers. However, in several cases, the arrival time or energy level fluctuation for the whole specimen is smaller than one of the fluctuations for the individual sections. Discussion of the cause of this phenomenon, with support from simulation results, is given in the companion paper.[26]

The values of the waveform similarity factor for each tissue specimen are also given in Table I. The values given indicate that propagation through fat causes greater wave shape distortion than does passage through muscle. The average wave shape distortion produced by propagation through the whole specimens is significantly greater than that found for one layer alone. Differences in arrival time or overall pulse amplitude do not significantly affect the waveform similarity factor; however, the waveform similarity factor decreases when frequency components are selectively removed from portions of the wavefront, as when energy is scattered out of the direct path during propagation. Thus, the increased wave shape distortion for fat layers suggests that more energy is scattered away from the main propagation direction by the fat layer than by the muscle layer.

Insertion losses for the measured specimens and their subsections are reported in Table II. Both the average total insertion loss and average loss per unit thickness (obtained by dividing the average insertion loss by the average thickness from Table I) are given for each specimen. These values indicate the power loss that can be expected on each passage of an ultrasonic beam through the abdominal wall or one of its layers in medical imaging. An average insertion loss of

TABLE II. Measured insertion loss values. The average and standard deviation for each specimen are shown together with values per unit thickness, obtained by dividing the average insertion loss by the average thickness from Table I.

Specimen	Layer	Average (dB)	Standard deviation (dB)	Average/Thickness (dB/cm)
	muscle	2.33	3.23	2.99
101	fat	4.61	1.97	3.55
	whole	10.19	4.14	4.90
	muscle	5.62	3.42	4.68
113	fat	16.68	1.81	9.37
	whole	15.91	3.59	5.34
	muscle	7.10	3.15	7.10
114	fat	6.71	2.71	3.83
	whole	8.16	2.12	2.97
	muscle	2.04	1.77	2.46
116	fat	4.20	2.71	4.42
	whole	7.57	3.69	4.25
	muscle	7.40	2.85	4.11
118	fat	8.52	2.82	5.96
	whole	11.94	0.92	3.70
	muscle	4.90	2.88	4.27
Mean	fat	8.14	2.40	5.43
	whole	10.75	2.89	4.23
	muscle	2.57	0.66	1.81
Standard	fat	5.08	0.47	2.39
deviation	whole	3.36	1.34	0.94

10.75 dB was measured for the six whole specimens. This amounts to a loss of 4.23 dB for each centimeter of tissue. Although the muscle and fat layers were nearly equally thick, on average, the fat layers caused a mean loss of 8.14 dB while the muscle layers reduced the power by 4.90 dB. The loss rate measured for the fat layers, at 5.43 dB/cm, was 27% higher than the rate of 4.27 dB/cm measured for the muscle sections.

The effect of the measured distortion on focal quality is evident in Fig. 6, which shows cross-sectional x-y images of the three-dimensional focal envelope along the plane of maximum amplitude in the axial (z) direction. These images are analogous to C-scan images of the effective point source employed in the distortion measurements. All focuses shown in Fig. 6 are much more aberrated than the corresponding water-path focus, shown in Fig. 7. The water-path focuses still show different focal widths in the array and elevation directions because the synthesized aperture is larger in the array direction than in the elevation direction. The corresponding B-scan images, shown for comparison in Fig. 8, show little aberration in the axial direction. In Fig. 6, both muscle and fat sections are seen to cause significant degradation of focus quality. The primary difference between focuses obtained through muscle layers and through fat layers is that significant anisotropy appears in the muscle-layer images. This anisotropy is associated with the preferred direction of muscle fibers relative to the receiving aperture; greater aberration generally occurs in the direction perpendicular to the muscle fibers. The focus images obtained through entire abdominal wall specimens show greater aberration, including features caused by both the muscle and fat sections.

Corrected focal images, obtained using time-shift compensation of delay profiles determined with the reference waveform method, are also shown in Figs. 6–8. Most of the focal images aberrated by muscle layers are improved by time-shift compensation more than those aberrated by fat layers. In particular, time-shift compensation appears to reduce sidelobe levels more dramatically for muscle layers than for fat layers. However, artifacts remaining in the corrected images for the entire abdominal wall are associated with aberrations due to both the muscle and fat layers. Time-shift compensation has little effect on the axial characteristics of the aberrated focuses or on any aspect of the water-path focuses.

The characteristics of the synthetically computed focuses are summarized in Table III. Data is included for focal images computed from wavefronts measured after propagation through each muscle layer, fat layer, and whole specimen. The average results for five water paths are also listed for comparison. In each case, results are given for both the original and time-shift compensated waveforms. Point resolution is characterized by the -10- and -20-dB effective widths in the x (azimuth), y (array), and z (axial) directions, while contrast resolution is characterized by the -10-dB peripheral energy ratio. The focal effective widths are generally greater in the y direction than the x direction because of the smaller size of the receiving array in the elevation direction. Focuses are also wider in both directions parallel to aperture than in the axial (time) direction, because the axial resolution depends on the pulse length rather than the aperture size.

Differences in focal spot size between the different specimens are small at -10 dB, but clearly evident at -20 dB. Focus aberration produced by muscle is, on the average, far greater than that produced by fat, although this distortion is considerably greater in directions perpendicular to the muscle fiber orientation. Aberration for the whole specimens is somewhat greater than for the muscle layers. However, time-shift compensation is much more effective for the waveforms distorted by muscle layers than for those that passed through only the fat. On the average, time-shift compensation improved the -20-dB widths for the muscle paths by 70.3% and 57.4% in the array and elevation directions, respectively. The corresponding improvements for the fat-layer paths were 48.1% and 13.1%, respectively. Time-shift compensation was so effective for the muscle layers that, although muscle layers exhibited greater time-shift distortion, the average x and y effective widths for corrected focuses were smaller for the muscle layers than the fat layers. Focuses obtained through water paths were affected only slightly by time-shift compensation, indicating that any time-delay differences associated with nonuniformities in the elements or electronics were small.

Time-shift compensation was also effective in reducing the size of the focuses obtained for the waveforms that had passed through the whole specimens. An average improve-

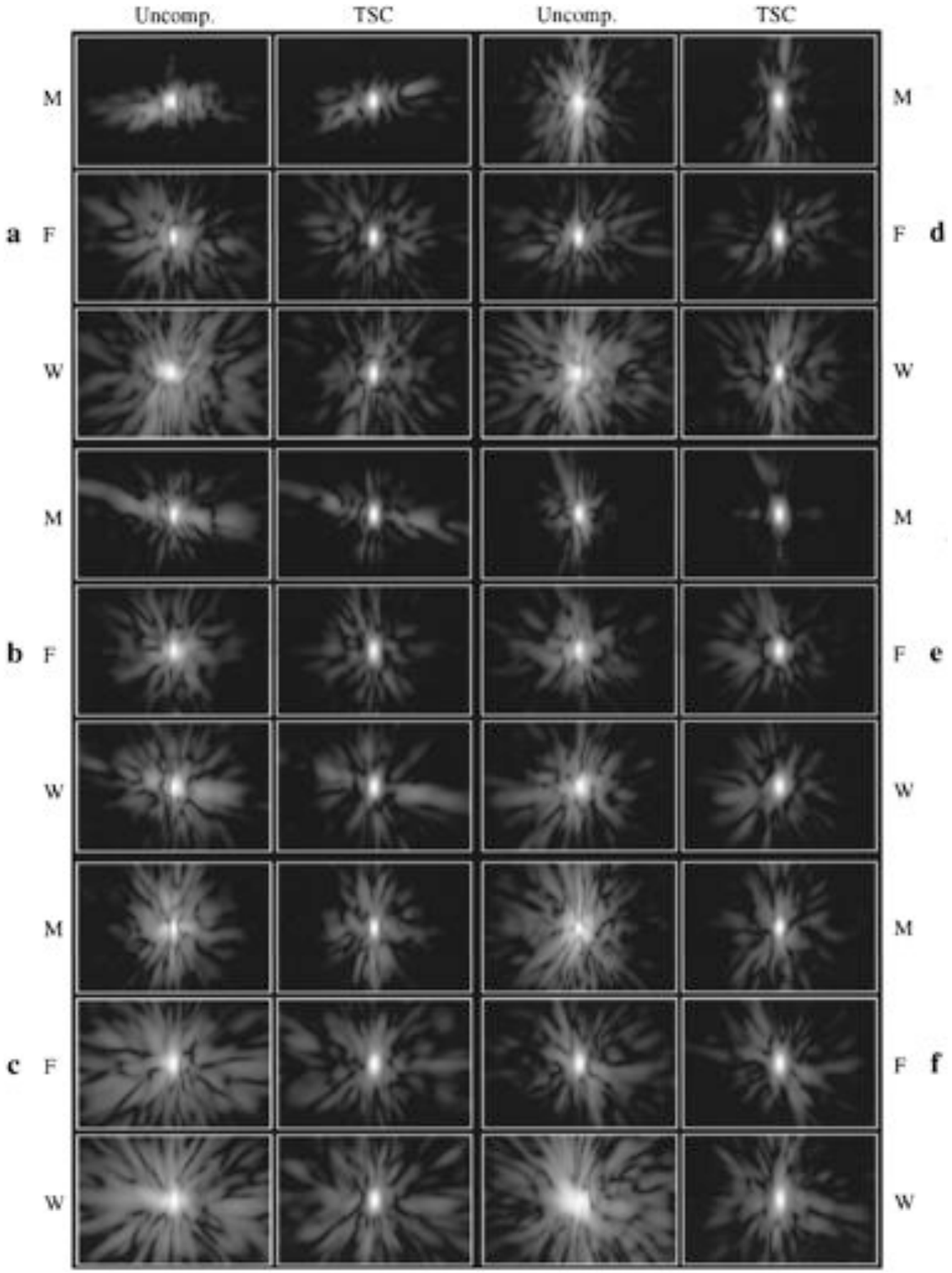

FIG. 6. Axial cross section (C-scan) images of synthetic focuses obtained from each entire specimen and its fat and muscle sections. Log-compressed analytic envelopes of each C-scan are shown on a 50-dB dynamic range for muscle layers (M), fat layers (F), and whole specimens (W). Both uncompensated (Uncomp.) and time-shift compensated (TSC) images are shown. Each panel spans 56.26 mm in the horizontal (array) direction and 37.50 mm in the vertical (elevation) direction. (a) Specimen 65. (b) Specimen 101. (c) Specimen 113. (d) Specimen 114. (e) Specimen 116. (f) Specimen 118.

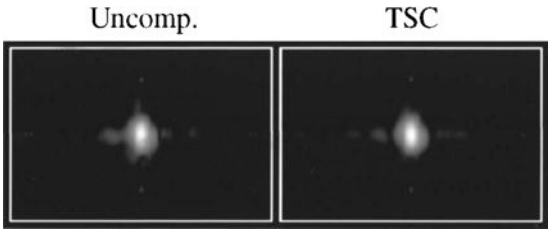

FIG. 7. Axial (C-scan) cross section images of synthetic focuses obtained through a representative water path. Images are shown in a format analogous to that of Fig. 6.

ment of about 73% was obtained in the array direction and 64% in the elevation direction. However, time-shift compensation alone is not sufficient to reduce the focus size of waveforms affected by whole specimens to the water-path limit. The −20-dB effective widths of the corrected focuses for the whole specimens average 12.1%, 18.0%, and 0.6% larger than the water path focuses in the array, elevation, and azimuth directions, respectively, so that the point resolution of these images was not corrected to the limits associated with the finite aperture size.

The −10-dB peripheral energy ratio is a measure of contrast resolution that can be used to compare the quality of focuses that are similar in width. Trends in these values generally follow the trends in focus size. That is, the average peripheral energy ratio is larger (indicating a greater portion of energy outside the main focal lobe) for the muscle layers than the fat layers, but whole specimens exhibit a larger peripheral energy ratio than either group of individual layers. After correction, the peripheral energy ratios for muscle layers and fat layers are comparable. However, the peripheral energy ratios for all tissue specimens are still significantly larger than those for the water paths before correction. Specifically, the peripheral energy ratios for the time-shift compensated muscle, fat, and whole specimens average 41.0%, 35.9%, and 76.9% larger than the average value for the uncompensated water paths.

IV. DISCUSSION

The effects of specific tissue features, noted also in the case of the chest wall,[33] are evident in the distortion maps shown here. Most notable are the white streaks (corresponding to locally delayed arrival of the wavefront) in the arrival time fluctuation maps that correspond to aponeuroses or fibrous connections in the rectus muscles. These features are apparent in the distortion maps of both the muscle and total specimens. The association of wavefront delays with these aponeuroses is explained by staining and pathological inspection, which indicate that these tissue structures are composed largely of fat in the specimens employed in this study. This is probably due to the age of the specimen donors in the current study; aponeuroses occurring in younger individuals may cause different distortion effects because more connective tissue and less fat may occur in these structures. Time-shift fluctuations associated with these aponeuroses clearly affect the focal images shown in Fig. 6. Aponeuroses were also found to degrade image quality in Ref. 5.

Other tissue features that clearly affect distortion characteristics and focus quality include fibrous muscle and septated fat. Muscle fibers cause anisotropy clearly visible in arrival time and energy level distortion maps; these maps appear similar to projections of the muscle fibers themselves. Aberrated focuses show analogous anisotropy, with greater distortion appearing perpendicular to the orientation of the muscle fibers. Fat layers caused distortion with granular characteristics similar to speckle in ultrasonic images, suggesting that the distortion is primarily caused by inhomogeneities such as high-contrast septa within the subcutaneous fat. This conclusion is supported by simulation results that have shown arrival time variations and scattering associated with septa[24–26] and by experimental results[34] that showed a strong correspondence between connective-tissue content and echogenicity in fatty tissue. Other connective tissue structures, such as the fibers that compose fascia and membranes between tissue layers, may also cause specific distortion features, but full understanding of these effects requires more complete analysis of dissected specimens.

Measured insertion losses were often significantly higher than attenuation values available in the literature (at 3.75 MHz, typically 1.8 dB/cm for fat, 4.1 dB/cm for muscle, and 5.9 dB/cm for connective tissue[24]). This was particularly true for the fat layers, for which an average insertion loss of 5.43 dB/cm was obtained. The values were also about two to three times higher than the estimated attenuation of 0.5 dB/cm/MHz commonly used in ultrasonic imaging of tissue. These discrepancies are most likely due to contributions of scattering to the measured insertion losses. Since insertion loss was determined from the peak value of the received waveform within a short time window, scattered energy that arrived after the initial wavefront was effectively

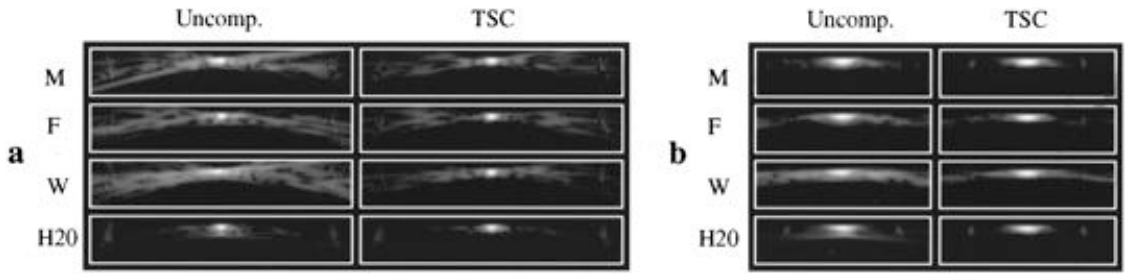

FIG. 8. Cross-section (B-scan) images of synthetic focuses obtained from specimen 65 and a representative water path measurement. (a) Cross section taken along the array direction, spanning 56.26 mm in width. (b) Cross section taken along elevation direction, spanning 37.50 mm in width. The vertical dimension in each panel spans 9.75 mm in the depth (axial) direction. Log-compressed analytic envelopes of focal waveforms are shown on a gray scale with a 50-dB dynamic range.

TABLE III. Focus properties for measured propagation. Effective widths are shown for the array (x), elevation (y), and axial (z) directions at levels of −10 and −20 dB. The peripheral energy ratios shown were computed using the −10-dB widths.

Specimen	Processing	Layer	−10-dB width (mm)			−20-dB width (mm)			Peripheral energy ratio
			x	y	z	x	y	z	
65	uncompensated	muscle	3.37	4.09	1.17	14.10	7.85	2.10	1.02
		fat	2.30	4.27	1.17	7.41	6.77	1.65	1.13
		whole	6.62	5.68	1.18	18.69	23.41	2.94	1.95
	tsc	muscle	2.30	4.09	1.19	4.54	6.15	1.63	0.59
		fat	2.18	4.20	1.18	3.20	6.08	1.58	0.52
		whole	2.21	4.65	1.22	4.12	7.16	1.68	0.72
101	uncompensated	muscle	2.45	4.51	0.99	8.50	6.98	1.40	1.11
		fat	3.20	4.71	0.97	7.94	8.17	1.40	0.76
		whole	3.28	4.98	0.91	5.86	8.18	1.48	1.38
	tsc	muscle	2.21	4.31	1.06	3.31	6.29	1.46	0.58
		fat	2.32	4.59	1.02	3.57	6.97	1.41	0.45
		whole	2.30	4.56	1.08	3.65	6.75	1.48	0.66
113	uncompensated	muscle	2.08	5.12	1.01	18.12	24.30	1.57	2.88
		fat	3.56	5.58	0.77	10.93	10.94	1.51	1.72
		whole	5.94	5.79	0.79	20.42	20.38	1.91	2.71
	tsc	muscle	2.12	4.29	1.07	3.48	6.72	1.47	0.70
		fat	2.73	4.99	1.11	4.44	8.52	1.52	0.72
		whole	2.62	4.86	1.11	4.10	7.72	1.50	0.81
114	uncompensated	muscle	3.74	6.90	0.87	7.88	22.51	1.40	0.96
		fat	2.34	4.57	1.01	4.72	7.18	1.58	0.67
		whole	4.06	8.50	0.87	13.21	36.72	2.67	2.72
	tsc	muscle	2.50	4.40	1.01	3.91	7.45	1.43	0.43
		fat	2.26	4.50	1.05	3.36	6.78	1.55	0.44
		whole	2.16	4.31	1.12	3.38	6.64	1.54	0.84
116	uncompensated	muscle	2.32	4.44	1.02	4.37	7.10	1.43	0.47
		fat	2.44	4.54	1.00	7.45	7.42	1.40	0.74
		whole	3.17	4.87	0.97	9.05	8.28	1.40	0.96
	tsc	muscle	2.24	4.21	1.02	3.47	6.27	1.43	0.32
		fat	2.30	4.31	1.01	3.86	6.45	1.41	0.44
		whole	2.45	4.50	1.02	4.15	6.81	1.42	0.44
118	uncompensated	muscle	8.10	6.41	0.90	22.13	28.21	1.98	3.08
		fat	2.46	4.98	0.74	4.91	8.26	1.87	0.97
		whole	10.15	8.96	1.18	18.56	22.86	2.49	1.25
	tsc	muscle	2.25	4.42	0.76	3.61	8.42	1.34	0.70
		fat	2.39	4.80	0.76	4.07	7.54	1.70	0.60
		whole	2.29	5.02	1.12	3.91	8.67	1.52	0.69
Mean	uncompensated	muscle	3.68	5.25	0.99	12.52	16.16	1.65	1.59
		fat	2.72	4.78	0.94	7.23	8.12	1.57	1.00
		whole	5.54	6.46	0.98	14.30	19.97	2.15	1.83
		water	2.22	4.18	1.04	3.47	6.18	1.51	0.39
	tsc	muscle	2.27	4.29	1.02	3.72	6.88	1.46	0.55
		fat	2.53	4.57	1.02	3.75	7.06	1.53	0.53
		whole	2.34	4.73	1.11	3.89	7.29	1.52	0.69
		water	2.22	4.18	1.04	3.41	6.14	1.48	0.32
Standard deviation	uncompensated	muscle	2.26	1.15	0.11	6.79	9.87	0.31	1.10
		fat	0.53	0.46	0.16	2.28	1.50	0.18	0.39
		whole	2.66	1.80	0.16	5.91	10.74	0.65	0.76
		water	0.03	0.03	0.02	0.08	0.07	0.09	0.03
	tsc	muscle	0.13	0.12	0.14	0.45	0.89	0.95	0.15
		fat	0.43	0.30	0.14	0.46	0.87	0.11	0.12
		whole	0.17	0.20	0.07	0.31	0.78	0.09	0.14
		water	0.03	0.04	0.02	0.10	0.08	0.06	0.01

lost. Small inhomogeneities such as septa scatter higher frequencies more strongly, so that the peak value used for the insertion loss measurement was further decreased by loss of high-frequency components from the incident pulse. The present method of measuring insertion loss is different from common *in vitro* methods for measuring frequency-dependent attenuation in tissue, which often employ long time windows.[28,35–37] In such measurements, the effect of scattering on the measured attenuation is reduced because time integration allows scattered energy arriving after the main pulse to contribute to the measured transmitted power, while in the current measurements, only energy scattered very near the forward direction can contribute to the measured peak waveform amplitude.

The importance of scattering effects to the measured insertion loss is further suggested by the large standard deviations in the measured insertion loss for each specimen; since the large-scale tissue structure of each specimen is largely uniform, absorption effects do not explain these spatial variations. Absorption effects also do not explain the result that the average insertion loss per unit thickness is smaller for whole specimens than for either muscle or fat layers. This phenomenon is likely to be associated with cumulative effects that occurred only in the case of whole specimens. The muscle layer, like most human tissues, exhibits frequency-dependent scattering and absorption effects, so that the wavefront exiting the muscle layer may have fewer temporal high-frequency components than the corresponding water-path wavefront. Since attenuation in the fat layer (due both to absorption and scattering) is smaller when high-frequency components are removed from the incident wavefront, the overall insertion loss per unit length can be lower for whole specimens than for either of the individual layers. Results shown in the companion simulation paper[26] provide quantitative estimates of the relative contributions of scattering and absorption to total attenuation.

Some previous workers have suggested that the subcutaneous fat layer[2,15,18] constitutes the main source of degradation in abdominal ultrasound imaging, while others[3,8,38,39] have shown that the abdominal muscle layer produces substantial distortion. The present study indicates that both layers significantly contribute to ultrasonic aberration, both through wavefront distortion and attenuation. However, the distortions produced by these layers have different characteristics and different implications for adaptive aberration correction. Distortion caused by fat layers was found here to be smaller than that caused by muscle layers, but the distortion caused by fat layers proved more difficult to correct by time-shift compensation. The negative effects of fat layers on ultrasonic images are exacerbated in obese patients, where thick layers of subcutaneous fat can cause much greater attenuation and distortion. On the average, muscle layers were found to produce greater arrival time fluctuations than fat layers. However, the measured muscle layers caused distortion with smaller energy level fluctuations and greater waveform similarity factors. These observations suggest that muscle layers scatter less than fat layers, and further imply that phase-screen models may be more appropriate for abdominal muscle layers than for the subcutaneous fat.

Another common assumption about ultrasonic aberration in the abdomen is that irregularly shaped boundaries between tissue layers are an important cause of wavefront distortion.[19,40] The results of the present study suggest that irregular boundaries are of less importance than internal tissue structures. As seen in Figs. 1 and 2, interfaces between muscle and fat layers are typically smooth rather than rough or rippled. Substantial distortion was measured here from both individual muscle and fat layers, even though these specimens contained no fat–muscle interfaces and lay flat in the tissue mount due to the natural weight and pliability of warm tissue. The features observed in time-shift and energy level distortion maps do not correspond to small variations that may occur in skin–fat or fat–muscle boundaries, but clearly resemble the internal structure of muscle and fat. More direct evidence regarding the relative importance of tissue-layer boundaries has been obtained using simulations and is presented in the companion paper.[26]

The characteristics of the experimental population require further comment. As noted above, the specimens used in this study came from older (mean age 71 years), nonobese individuals. It is therefore likely that the muscle in these specimens was poorly toned and that the subcutaneous fat layers were thinner than is common among the general population. This suggests that the distortion measured here for both the muscle and fat layers is lower than might be found in general. Therefore, the results described here should be considered a lower bound for distortion produced by the general population. Since fat seems to scatter more ultrasonic energy than does muscle, distortion produced by extremely obese patients can be expected not only to be greater but also more difficult to correct than the distortion produced by nonobese patients. Although the signal power could be increased to compensate for the absorption of ultrasound in fat, aberration caused by scattering effects presents a more challenging problem for adaptive imaging. More complicated algorithms than simple time-shift compensation in the aperture are most likely required if the effects of scattering are to be removed.

Distortion measured in the current study may be somewhat different from that which occurs *in vivo*, in part because of the finite distance between the tissue and receiver. Propagation in a homogeneous medium such as water causes a spatial low-pass filtering effect,[41] so that some spatial fluctuations in the wavefront are smoothed during propagation from the specimen to the receiving transducer array. The result of this effect, which is unrelated to any frequency-dependent absorption that may occur, is that distortion may be somewhat underestimated by the current measurements. However, *in vivo* wavefront distortion may also be reduced by the common clinical practice of pressing the ultrasonic probe tightly against the body wall. Since the static behavior of tissue is similar to that of an incompressible fluid surrounded by a pliable boundary, the applied pressure decreases the ultrasonic propagation path length through the abdominal wall and may also move some fat lobules and septa outside the acoustic path, reducing wavefront distortion caused by scattering. This pressure may also anisotropically align structures such as septa so that scattering effects are

further decreased (less scattering occurs, for instance, when septa are aligned perpendicular to the direction of propagation[24]).

The present results for correction of aberrated focal images have strong implications for the design of adaptive ultrasonic imaging methods. The results show that both fat and muscle layers cause aberration that cannot be completely corrected by simple time-shift compensation of received wavefronts, so that neither layer can be accurately modeled as a phase screen at the receiving aperture. Aberration caused by the muscle layers was correctable to a greater extent than that caused by the fat layers, implying that the phase screen model is more appropriate for muscle layers. The muscle layer may be more appropriately modeled by a phase screen some distance from the aperture,[12,14] but the fat layer is unlikely to be accurately modeled by any single phase screen because of the strong, distributed, depth-dependent scattering that occurs within the subcutaneous fat. Models employing multiple phase screens may model propagation through the abdominal wall more accurately; however, it remains to be seen whether application of such models can significantly improve correction algorithms without introducing computational complexity comparable to full-wave propagation models.

V. CONCLUSIONS

Measurements of distortion made using human abdominal wall specimens and their individual fat and muscle layers have shown that both fat and muscle cause significant wavefront and focus distortion. The spatial characteristics of the resulting distortion are directly related to internal tissue structure. The results imply that distortion caused by ultrasonic propagation through the abdominal wall is due to a more complex combination of effects than previously supposed by many researchers and clinicians.

On the whole, muscle layers cause greater arrival time distortion but less energy level and waveform distortion than fat layers. The ordered, fibrous structure of muscle causes greater anisotropy in observed distortion patterns and aberrated focal images. Distortion caused by muscle layers is corrected fairly well by time-shift compensation, implying that phase-screen models may be useful in correction of aberration caused by muscle layers.

Fat layers cause smaller arrival time distortion but greater energy level and waveform distortion. These results, as well as the random isotropic appearance of distortion patterns and the highly variable insertion loss measured for fat layers, imply that scattering from septa is the primary cause of wavefront distortion in the subcutaneous fat. Focus aberration caused by fat layers is corrected less completely by time-shift compensation than is distortion caused by muscle layers. For these reasons, phase-screen models and homogeneous-layer models are both insufficient to depict distortion caused by fat layers of the abdominal wall.

Distortion caused by entire abdominal wall specimens has been shown to be a combination, but not a simple summation, of distortion effects caused by muscle and fat layers. This result suggests that aberration correction algorithms based on single phase-screen models do not provide optimum compensation for distortion caused by the human abdominal wall. Likewise, algorithms that employ homogeneous-layer models of tissue layers cannot effectively correct for structure-dependent effects that cause much of the distortion observed here.

ACKNOWLEDGMENTS

Michael J. Orr is thanked for assisting with the measurements and data analysis. Dong-Lai Liu is thanked for providing the distortion estimation software using the reference waveform method and for significantly improving the measurement control software. Funding for this investigation was provided by the University of Rochester Diagnostic Ultrasound Research Laboratory Industrial Associates, NIH Grants DK 45533, HL 50855, and CA 74050, and US Army Grant DAMD-17-94-J-4384. Computations were performed in part at the Center for Academic Computing of the Pennsylvania State University and at the Cornell National Supercomputing Facility, which was supported in part by the National Science Foundation, New York State, and the IBM Corporation.

[1] Frederick Kremkau, personal communication, August 1997.
[2] W. Fiegler, R. Felix, M. Langer, and E. Schultz, ''Fat as a factor affecting resolution in diagnostic ultrasound: possibilities for improving picture quality,'' Eur. J. Radiol. **5**, 304–309 (1985).
[3] L. A. Ødegaard, ''Phase aberration correction in medical ultrasound imaging,'' Ph.D. thesis, University of Trondheim, Trondheim, Sweden, 1995.
[4] D. A. Carpenter, G. Kossoff, and K. A. Griffiths, ''Correction of distortion in US images caused by subcutaneous tissues: results in tissue phantoms and human subjects,'' Radiology **195**, 563–567 (1995).
[5] A. Shmulewitz, S. A. Teefey, and B. S. Robinson, ''Factors affecting image quality and diagnostic efficacy in abdominal sonography: a prospective study of 140 patients,'' J. Clin. Ultrasound **21**, 623–630 (1993).
[6] U. Haberkorn, G. Layer, V. Rudat, I. Zuna, A. Lorenz, and G. van Kaick, ''Ultrasound image properties influenced by abdominal wall thickness and composition,'' J. Clin. Ultrasound **21**, 423–429 (1993).
[7] B. S. Robinson, A. Shmulewitz, and T. M. Burke, ''Waveform aberrations in an animal model,'' 1994 IEEE Ultrason. Symp. Proc. **3**, 1619–1624 (1994).
[8] T. Noda, A. Iida, K. Murakami, and T. Shimura, ''Basic investigation of a wavefront distortion correction method due to velocity inhomogeneities,'' Jpn. J. Medical Elect. Biol. Eng. **32** (Supplement), 119 (1994) (abstract, in Japanese).
[9] M. O'Donnell and S. W. Flax, ''Phase-aberration correction using signals from point reflectors and diffuse scatterers: Measurements,'' IEEE Trans. Ultrason. Ferroelectr. Freq. Control **35**, 768–774 (1988).
[10] D. Rachlin, ''Direct estimation of aberrating delays in pulse-echo imaging systems,'' J. Acoust. Soc. Am. **88**, 191–198 (1990).
[11] D.-L. Liu and R. C. Waag, ''Time-shift compensation of ultrasonic pulse force degradation using least-mean-square error estimates of arrival time,'' J. Acoust. Soc. Am. **95**, 542–555 (1994).
[12] D.-L. Liu and R. C. Waag, ''Correction of ultrasonic wavefront distortion using backpropagation and a reference waveform method for time-shift compensation,'' J. Acoust. Soc. Am. **96**, 649–660 (1994).
[13] C. Dorme and M. Fink, ''Ultrasonic beam steering through inhomogeneous layers with a time reversal mirror,'' IEEE Trans. Ultrason. Ferroelectr. Freq. Control **43(1)**, 167–175 (1996).
[14] A. P. Berkhoff and J. M. Thijssen, ''Correction of concentrated and distributed aberrations in medical ultrasound imaging,'' 1996 IEEE Ultrasonics Symp. Proc. **2**, 1405–1410 (1996).
[15] G. C. Ng, P. D. Freiburger, W. F. Walker, and G. E. Trahey, ''A speckle target adaptive imaging technique in the presence of distributed aberrations,'' IEEE Trans. Ultrason. Ferroelectr. Freq. Control **44(1)**, 140–151 (1997).
[16] S. W. Smith, G. E. Trahey, and O. T. von Ramm, ''Phased array ultra-

sound imaging though planar tissue layers,'' Ultrasound Med. Biol. **12**(3), 229–243 (1986).
[17] G. Kossoff, D. A. Carpenter, D. E. Robinson, D. Ostry, and P. L. Ho, ''A sonographic technique to reduce beam distortion by curved interfaces,'' Ultrasound Med. Biol. **15**(4), 375–382 (1989).
[18] L. Nock, G. E. Trahey, S. W. Smith, ''Phase aberration correction in medical ultrasound using speckle brightness as a quality factor,'' J. Acoust. Soc. Am. **85**, 1819–1833 (1989).
[19] L. A. Ledoux, A. P. Berkhoff, and J. M. Thijssen, ''Ultrasonic wave propagation through aberrating layers: experimental verification of the conjugate gradient Rayleigh method,'' IEEE Trans. Ultrason. Ferroelectr. Freq. Control **43**(1), 158–166 (1996).
[20] M. Kunin, ''Bridging septa of the perinephric space: anatomic, pathologic, and diagnostic considerations,'' Radiology **158**, 361–365 (1986).
[21] R. Warwick and P. L. Williams (eds.), *Gray's Anatomy* (Saunders, Philadelphia, 1973), 35th ed. pp. 488–490, 519–527.
[22] J. L. Matthews and J. H. Martin, *Atlas of Human Histology and Ultrastructure* (Lea & Febiger, Philadelphia, 1971), pp. 54–55, 102–119.
[23] L. M. Hinkelman, ''Ultrasonic pulse wavefront distortion produced by abdominal and chest wall,'' Proc. 10th Ann. Univ. Rochester Diagnostic Ultras. Res. Lab. Indust. Assoc. Mtg. 8–25 (1993).
[24] T. D. Mast, L. M. Hinkelman, M. J. Orr, V. W. Sparrow, and R. C. Waag, ''Simulation of ultrasonic pulse propagation through the abdominal wall,'' J. Acoust. Soc. Am. **102**, 1177–1190 (1997).
[25] T. D. Mast, L. M. Hinkelman, M. J. Orr, V. W. Sparrow, and R. C. Waag, ''Erratum: 'Simulation of ultrasonic pulse propagation through the abdominal wall' [J. Acoust. Soc. Am. **102**, 1177–1190 (1997)],'' J. Acoust. Soc. Am. **104**, 1124–1125 (1998).
[26] T. D. Mast, L. M. Hinkelman, M. J. Orr, and R. C. Waag, ''The effect of abdominal wall morphology on ultrasonic pulse distortion, Part II. Simulations,'' J. Acoust. Soc. Am. **104**, 3651–3664 (1998).
[27] H. Gray, *Gray's Anatomy*, edited by T. P. Pick and R. Howden (Gramercy, New York, 1977), pp. 358–364 (facsimile of 1901 American edition of *Anatomy, Descriptive and Surgical*).
[28] J. A. Campbell, ''Measurements of Ultrasonic Differential and Total Scattering Cross Sections for Tissue Characterization,'' Ph.D. thesis, University of Rochester, 1984.
[29] Y. Sumino and R. C. Waag, ''Measurements of ultrasonic pulse arrival time differences produced by abdominal wall specimens,'' J. Acoust. Soc. Am. **90**, 2924–2930 (1991).
[30] L. M. Hinkelman, D.-L. Liu, L. A. Metlay, and R. C. Waag, ''Measurements of ultrasonic pulse arrival time and energy level variations produced by propagation through abdominal wall,'' J. Acoust. Soc. Am. **95**, 530–541 (1994).
[31] L. M. Hinkelman, D.-L. Liu, R. C. Waag, Q. Zhu, and B. D. Steinberg, ''Measurement and correction of ultrasonic pulse distortion produced by the human breast,'' J. Acoust. Soc. Am. **97**, 1958–1969 (1995).
[32] A. D. Pierce, *Acoustics: an Introduction to its Physical Principles and Applications* (Acoustical Society of America, Woodbury, NY, 1989), 2nd. ed.
[33] L. M. Hinkelman, T. L. Szabo, and R. C. Waag, ''Measurements of ultrasonic pulse distortion produced by the human chest wall,'' J. Acoust. Soc. Am. **101**, 2365–2373 (1997).
[34] R. C. Sanders, ''Sonography of Fat,'' in *Ultrasound Annual 1984*, edited by R. C. Sanders and M. Hill (Raven, New York, 1984), pp. 71–94.
[35] R. C. Chivers and R. J. Parry, ''Ultrasonic velocity and attenuation in mammalian tissues,'' J. Acoust. Soc. Am. **63**, 940–953 (1978).
[36] S. A. Goss, R. L. Johnston, and F. Dunn, ''Comprehensive compilation of empirical ultrasonic properties of mammalian tissues,'' J. Acoust. Soc. Am. **64**, 423–457 (1978).
[37] S. A. Goss, R. L. Johnston, and F. Dunn, ''Compilation of empirical ultrasonic properties of mammalian tissues II,'' J. Acoust. Soc. Am. **68**, 93–108 (1980).
[38] P. Krämmer and D. Hassler, ''Measurements of spatial time-of-flight fluctuations of; ultrasound pulses passing through inhomogeneous layers,'' 1987 IEEE Ultrasonics Symp. Proc. **2**, 939–942 (1987).
[39] M. Van den Aarssen, W. A. Verhoef, and J. M. Thijssen, ''Influence of absorbing and scattering media on the propagation of ultrasound,'' J. Acoust. Soc. Am. **85**, 567–575 (1989).
[40] H. Wang, E. S. Ebbini, M. O'Donnell, and C. A. Cain, ''Phase aberration correction and motion correction for ultrasonic hyperthermia phased arrays: experimental results,'' IEEE Trans. Ultrason. Ferroelectr. Freq. Control **41**(1), 34–43 (1994).
[41] J. W. Goodman, *Introduction to Fourier Optics* (McGraw-Hill, San Francisco, 1968), Chap. 3.